Electronic Supplementary Material (ESI) for Journal of Materials Chemistry A
This journal is © The Royal Society of Chemistry 2022

Supplementary Information

Aqueous Eutectic Hydrogel Electrolytes Enable Flexible Thermocells with Wide Operation Temperature Range

Peng Peng,[a] Zhao Li,[b] Daibin Xie,[a] Kaihua Zhu,[a] Chunyu Du,[a] Lirong Liang,[a] Zhuoxin Liu*[a] and Guangming Chen*[a]

[a] College of Materials Science and Engineering, Shenzhen University, Shenzhen, 518055, China. E-mail: chengm@szu.edu.cn, liuzhuoxin@szu.edu.cn

[b] Department of Civil and Environmental Engineering, Villanova University, Villanova, Pennsylvania 19085, United States

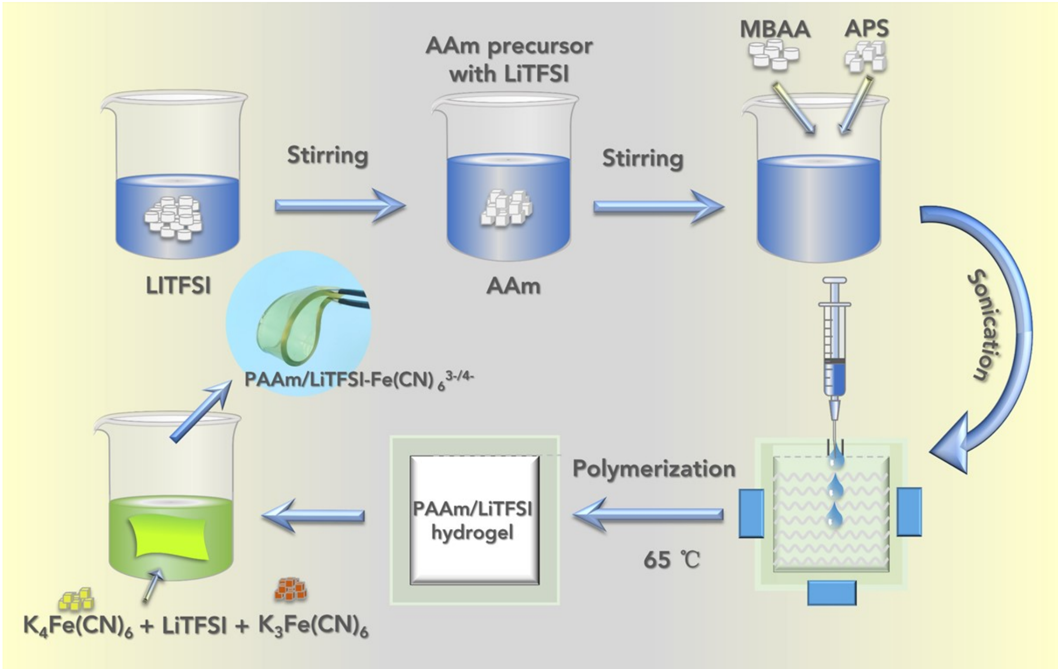

Supplementary Fig. S1. Preparation process of the hydrogel electrolyte, including the polymerization of PAAm and the ion exchange with $Fe(CN)_6^{3-/4-}$. The solution for ion exchange contained the same molarity of LiTFSI as the hydrogel, so that the LiTFSI concentration would stay constant after ion exchange.

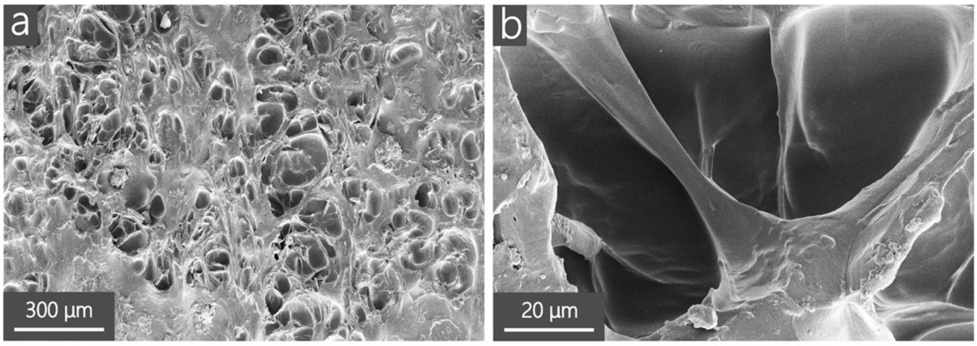

Supplementary Fig. S2. SEM images of the PAAm hydrogel at the magnification of (a) 250 and (b) 3000.

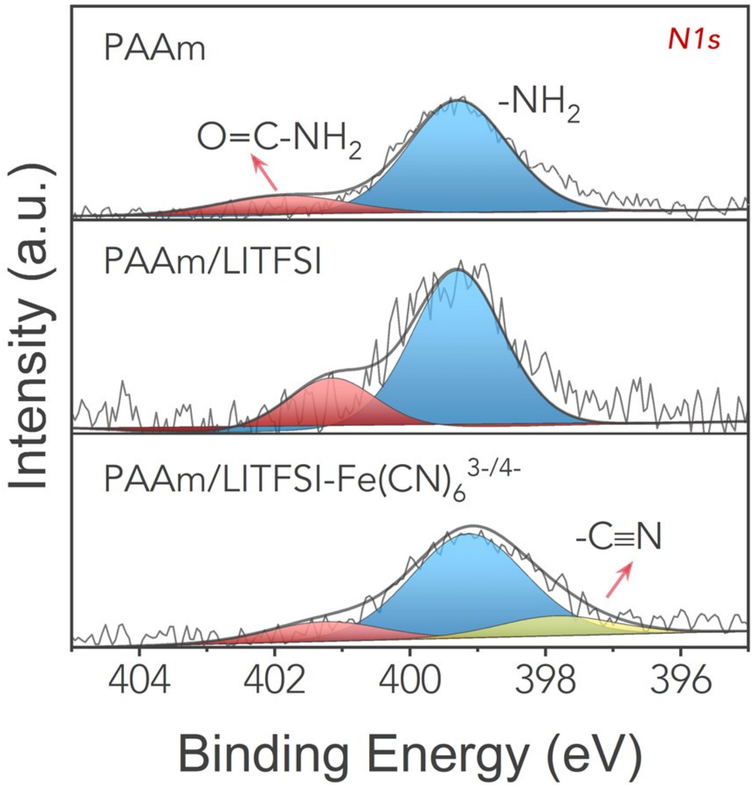

Supplementary Fig. S3. XPS N1s spectra of various hydrogel samples.

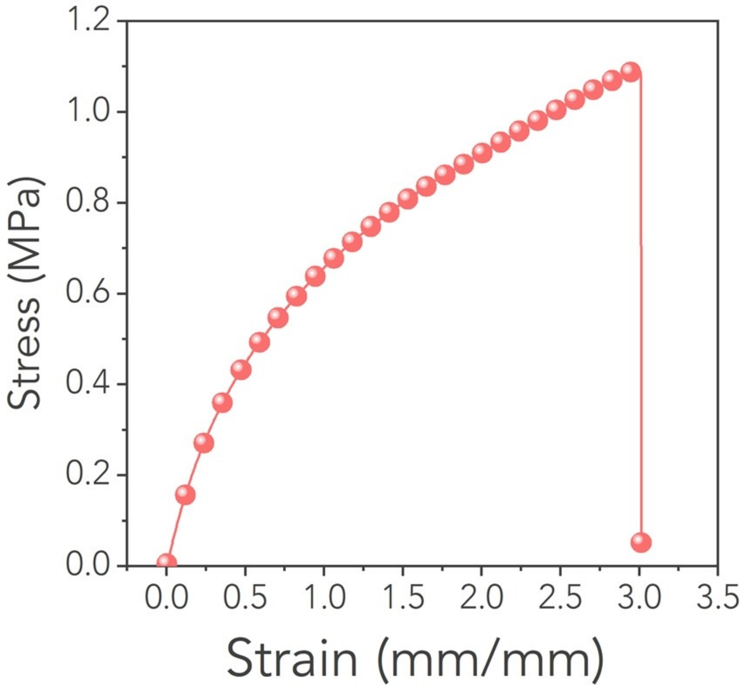

Supplementary Fig. S4. Stress-strain curve of the hydrogel electrolyte.

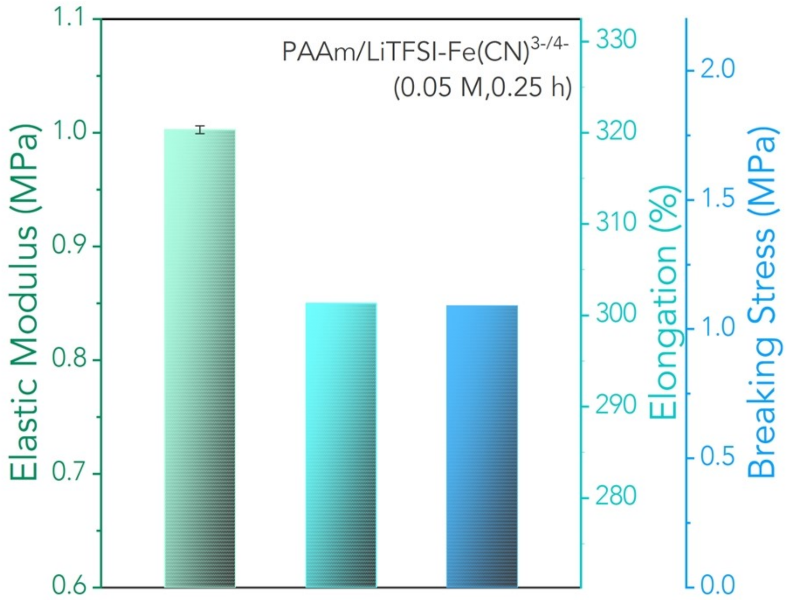

Supplementary Fig. S5. Mechanical properties of the hydrogel electrolyte.

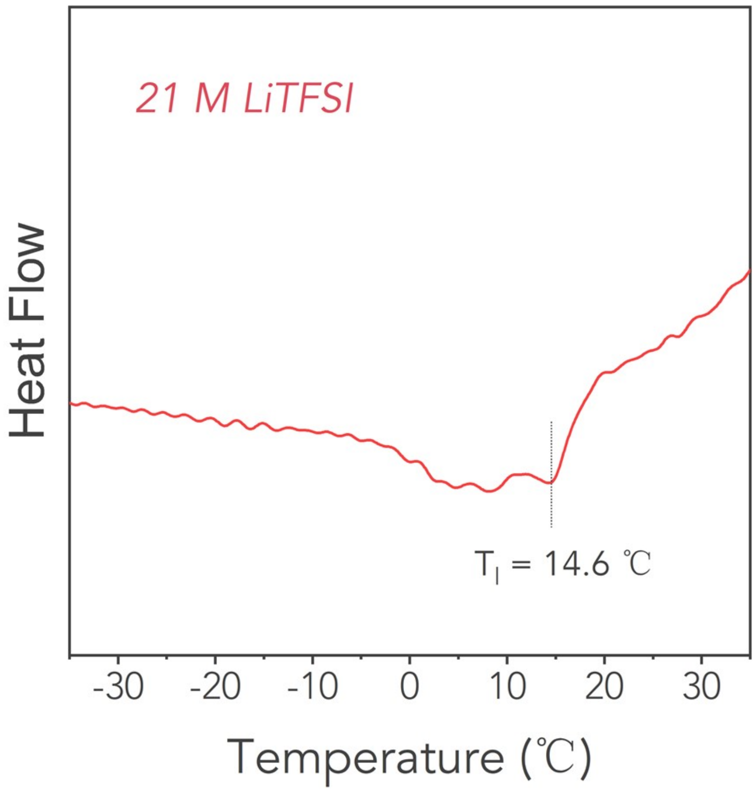

Supplementary Fig. S6. DSC curve showing the liquidous temperature of the 21 M LiTFSI solution (without the addition of $Fe(CN)_6^{3-/4-}$).

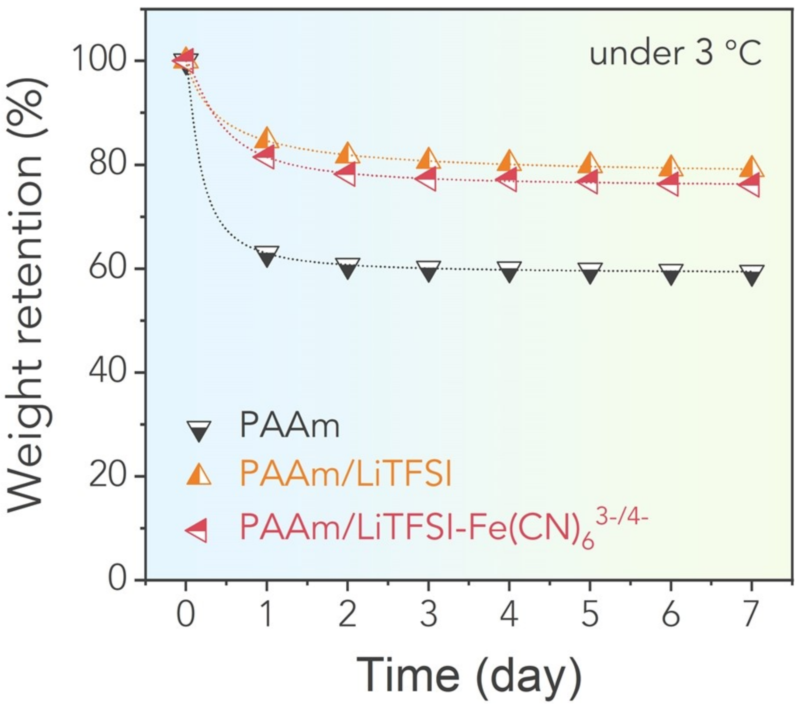

Supplementary Fig. S7. The weight retention of various hydrogels during the 7-day exposure under 3 °C.

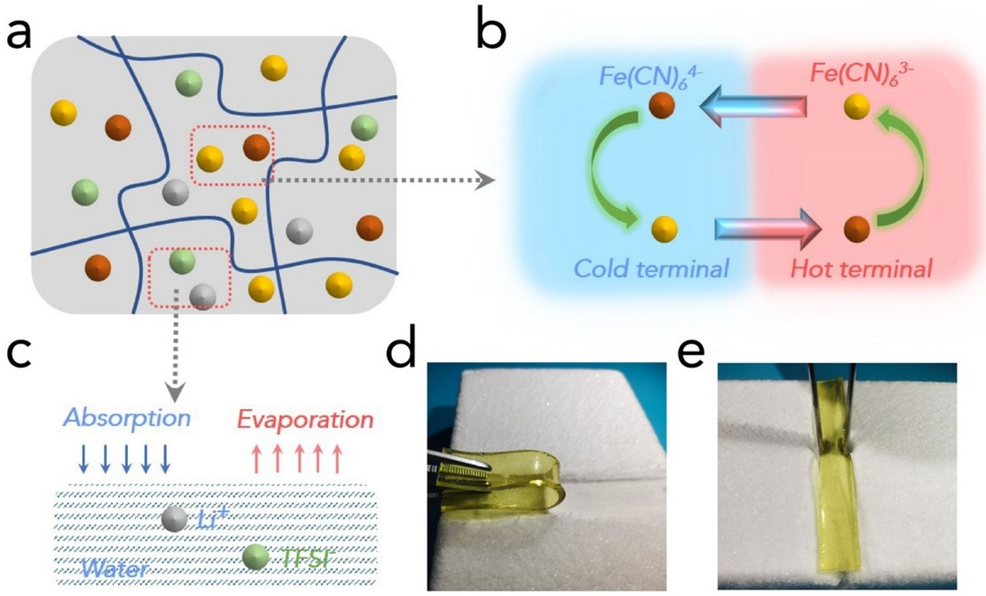

Supplementary Fig. S8. (a) Schematic of the structure of the PAAm/LiTFSI-$Fe(CN)_6^{3-/4-}$ hydrogel electrolyte. (b) Redox reaction illustration at hot and cold terminals. (c) The moisture equilibrium can be achieved via water absorption and evaporation within the hydrogel electrolyte owing to the existence of high-concentration LiTFSI. (d) Photograph of the hydrogel electrolyte being folded in half on an ice surface. (e) Photograph of the hydrogel electrolyte being squeezed on an ice surface. Note: the ice was on-site grown with the presence of the hydrogel electrolyte, and the growing temperature was −15 °C. The hydrogel electrolyte maintained hydrated and soft throughout the ice growing process.

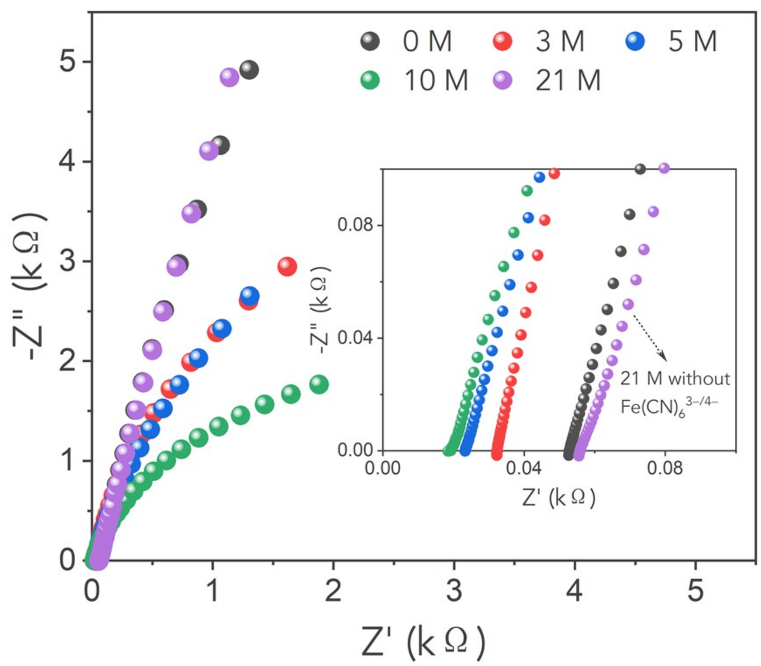

Supplementary Fig. S9. EIS spectra of various hydrogel samples under room temperature.

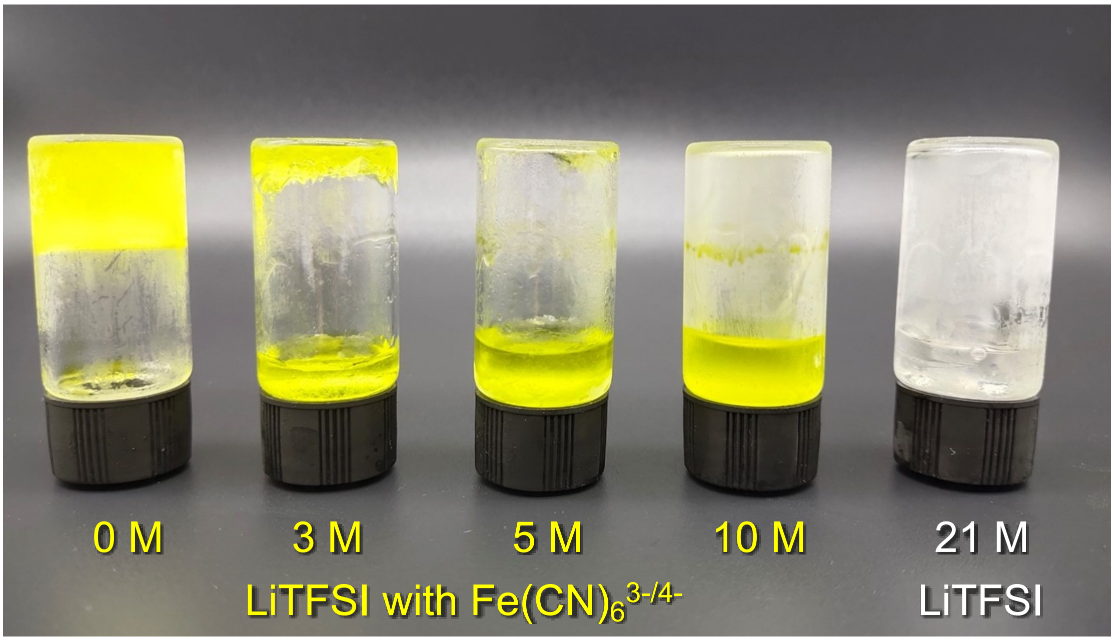

Supplementary Fig. S10. Photograph of various liquid electrolytes after freezing at −18 °C.

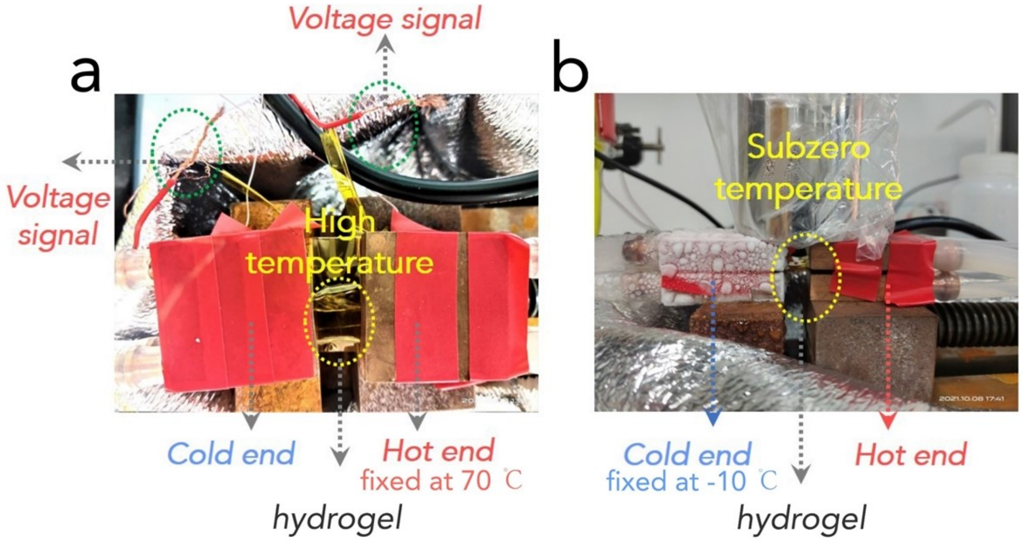

Supplementary Fig. S11. Photos showing the self-established apparatus for the measuring of thermoelectrochemical Seebeck coefficient of the PAAm/LiTFSI-$Fe(CN)_6^{3-/4-}$ hydrogel electrolyte-based TEC, which were placed under (a) high temperature and (b) subzero temperature environmental conditions.

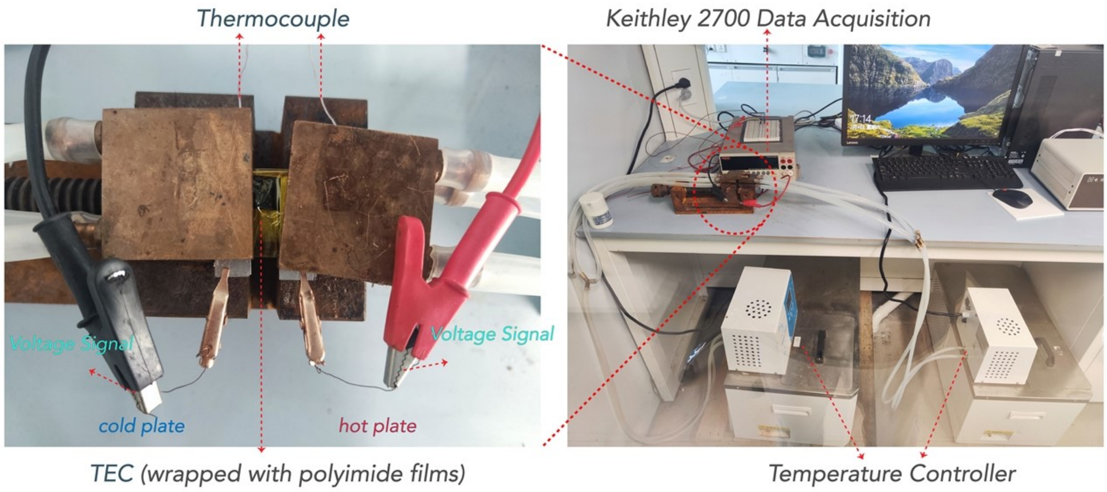

Supplementary Fig. S12. Photos showing the self-established apparatus, including the heating plates, data acquisition system, and the temperature controllers.

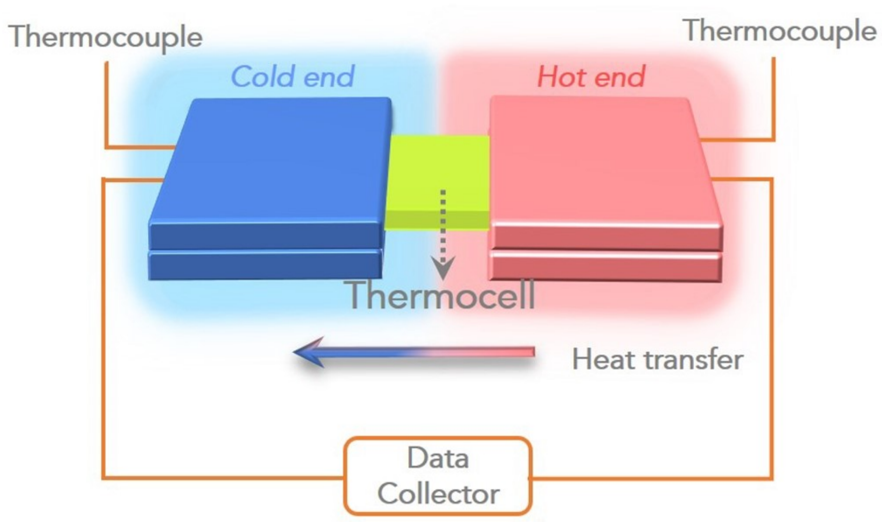

Supplementary Fig. S13. Schematic of the thermoelectrochemical measuring process for the TEC based on PAAm/LiTFSI-$Fe(CN)_6^{3-/4-}$ hydrogel electrolyte.

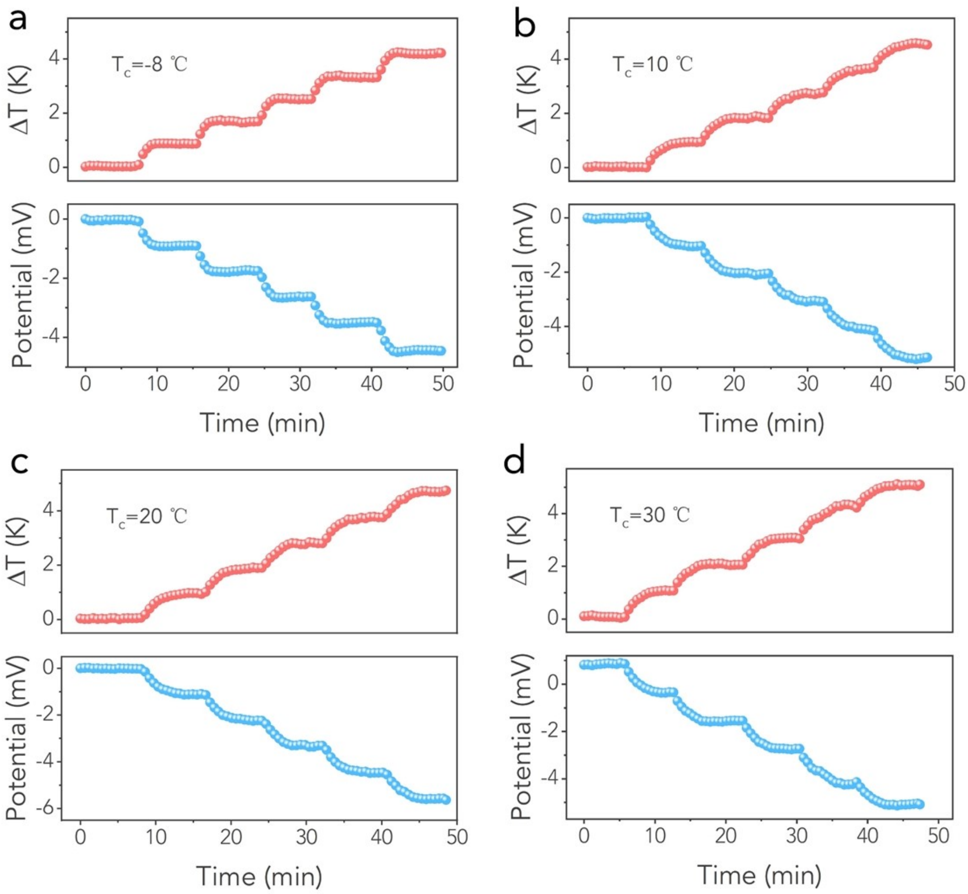

Supplementary Fig. S14. The potential curve varied with temperature difference when the cold end of the TEC was fixed under (a) −8 °C, (b) 10 °C, (c) 20 °C and (d) 30 °C. The temperature differences were induced by increasing the temperature of the hot end step by step, *i.e.*, $\Delta T = T_h - T_c$ (fixed).

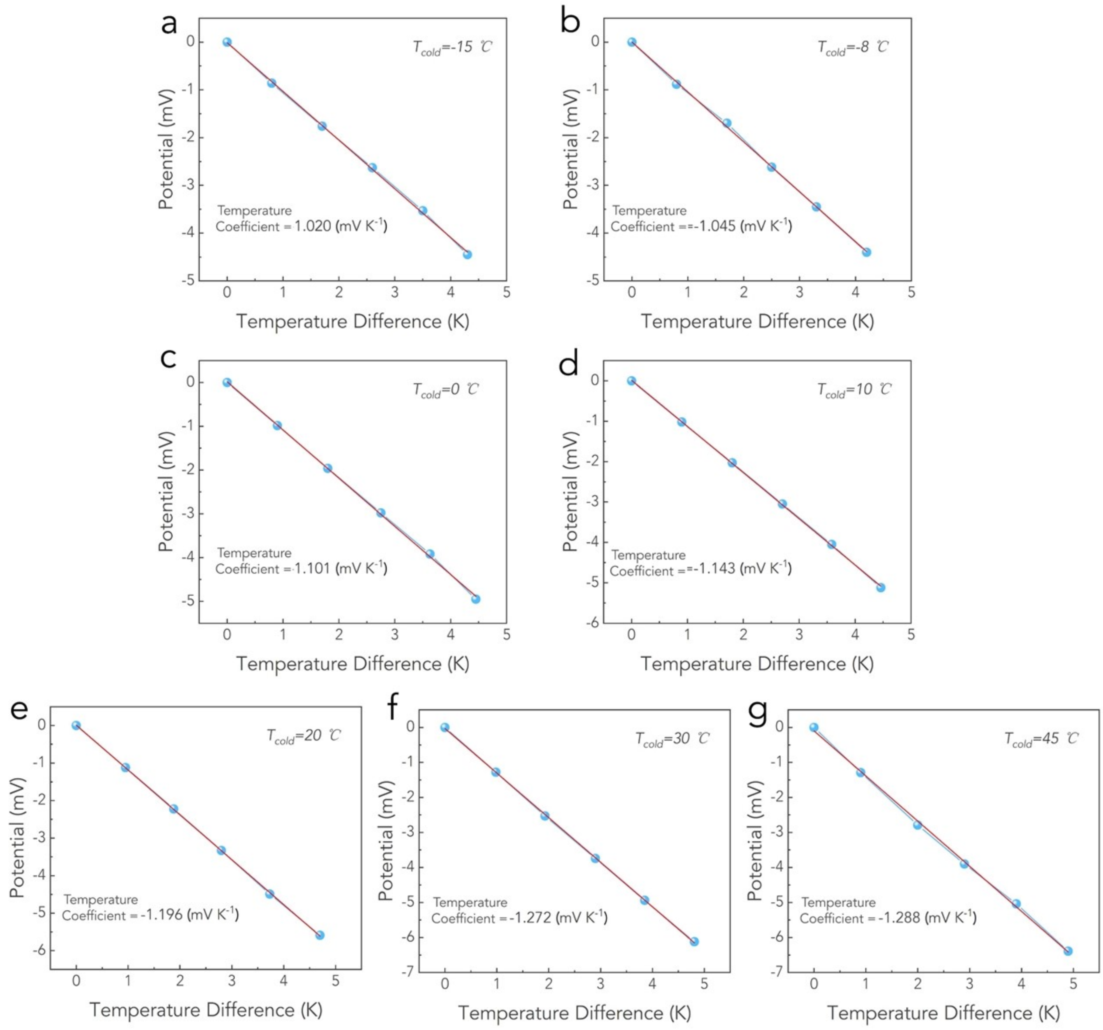

Supplementary Fig. S15. The thermoelectrochemical Seebeck coefficient fitting curve obtained when the cold end of the TEC was fixed under (a) −15 °C, (b) −8 °C, (c) 0, (d) 10 °C, (e) 20 °C, (f) 30 °C and (g) 45 °C. The temperature differences were induced by increasing the temperature of the hot end step by step, *i.e.*, $\Delta T = T_h - T_c$ (fixed).

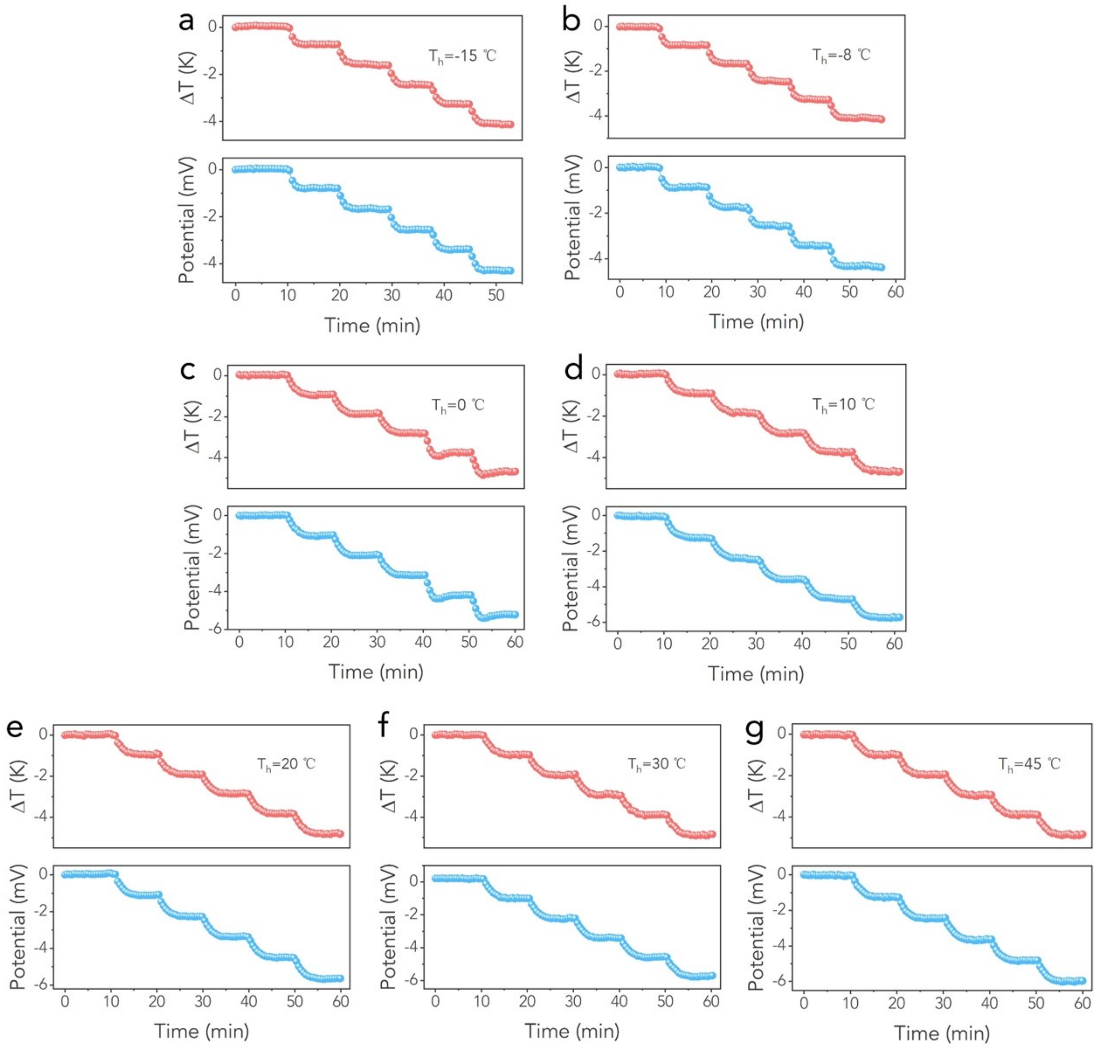

Supplementary Fig. S16. The potential curve varied with temperature difference when the cold end of the TEC was fixed under (a) −15 °C, (b) −8 °C, (c) 0, (d) 10 °C, (e) 20 °C, (f) 30 °C and (g) 45 °C. The temperature differences were induced by decreasing the temperature of the cold end step by step, *i.e.*, $\Delta T = T_h$ (fixed) − T_c.

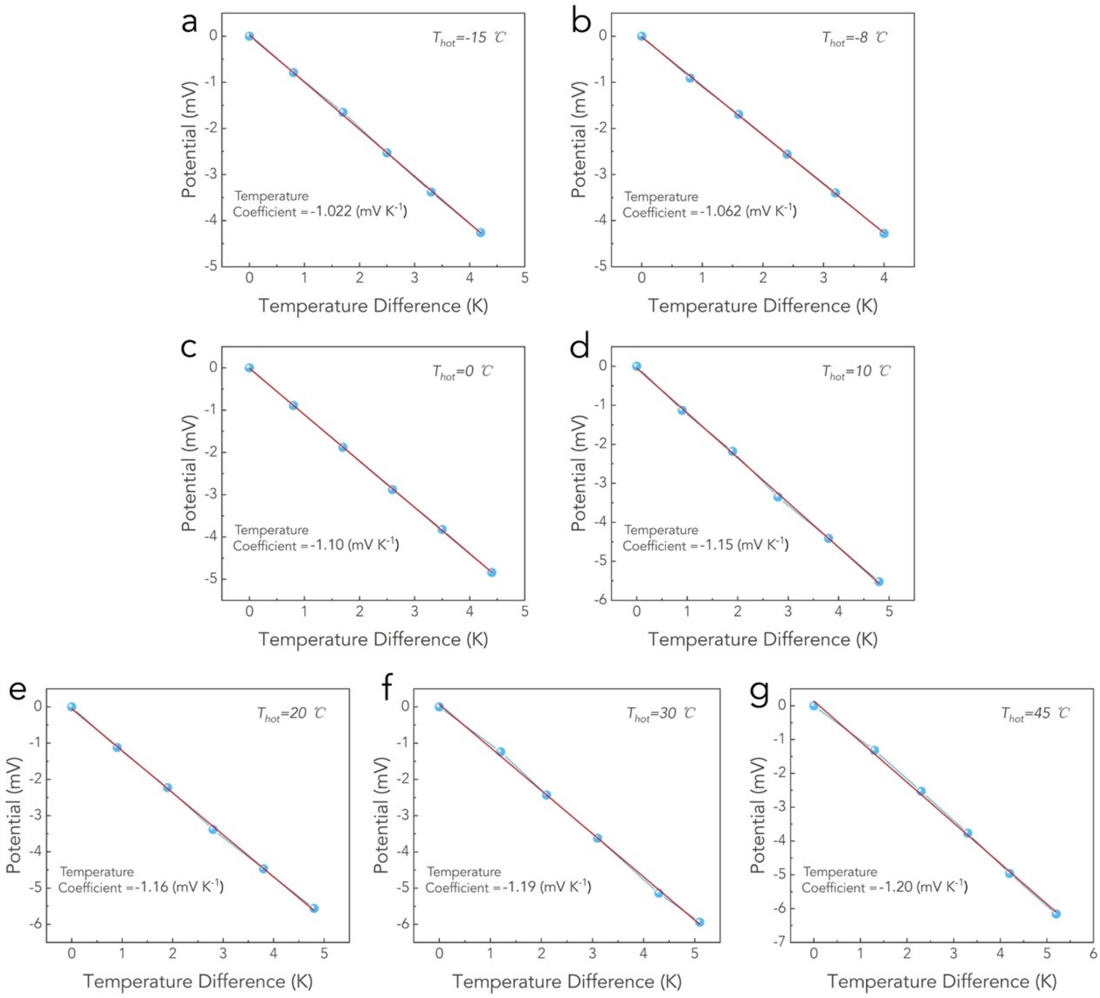

Supplementary Fig. S17. The temperature coefficient fitting curve obtained when the hot end of the TEC was fixed under (a) −15 °C, (b) −8 °C, (c) 0, (d) 10 °C, (e) 20 °C, (f) 30 °C and (g) 45 °C. The temperature differences were induced by decreasing the temperature of the cold end step by step, *i.e.*, $\Delta T=T_h$ (fixed) − T_c.

Electronic Supplementary Material (ESI) for Journal of Materials Chemistry A

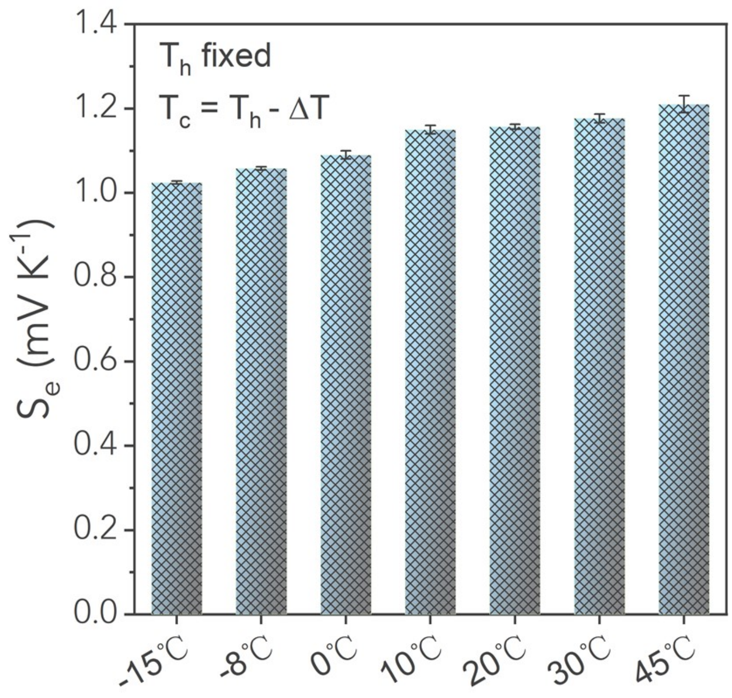

Supplementary Fig. S18. The Seebeck coefficient of the TEC under various temperatures. When measuring, the hot end of the TEC was fixed at the given temperature, and the temperature differences were induced by decreasing the temperature of the cold end step by step, *i.e.*, $\Delta T = T_h$ (fixed) − T_c.

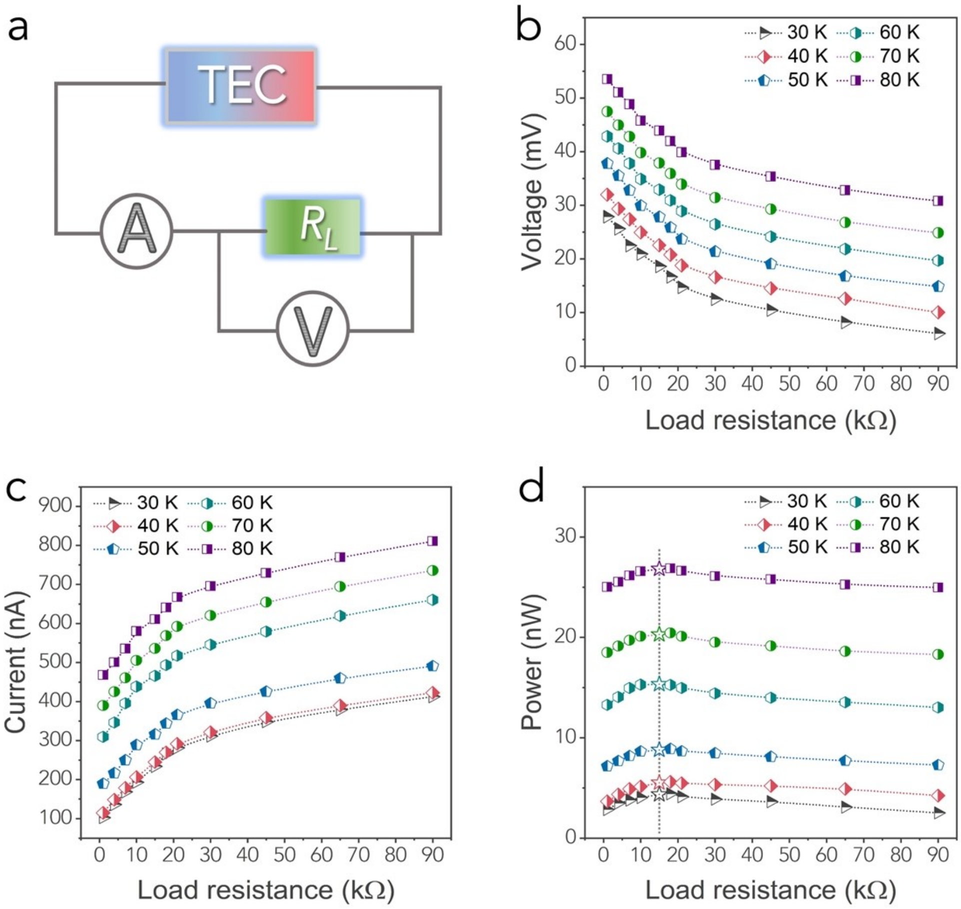

Supplementary Fig. S19. (a) Schematic illustration of the circuit connection. (b) Output voltage *vs* load resistance of the TEC under various temperature differences. (c) Output current *vs* load resistance of the TEC under various temperature differences. (d) Output power *vs* load resistance of the TEC under various temperature differences.

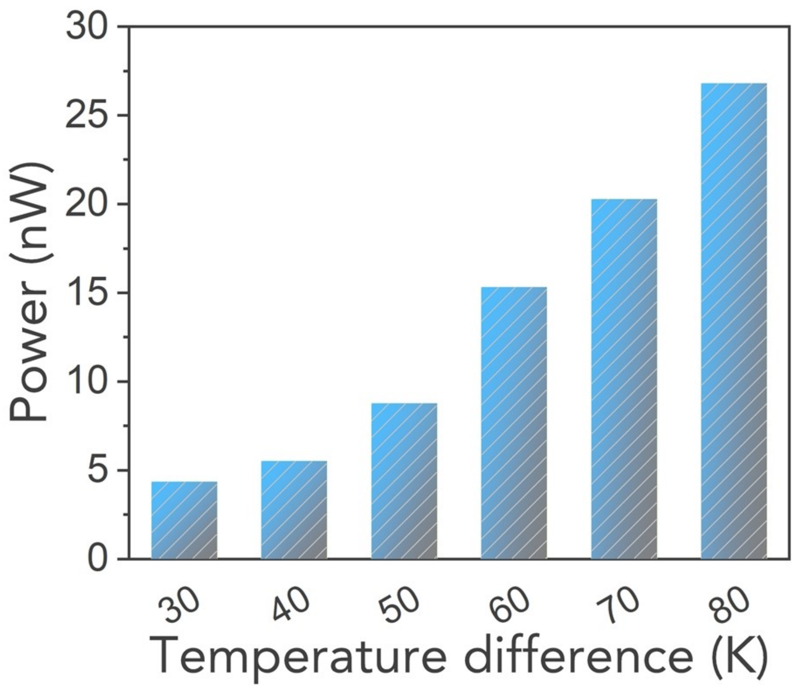

Supplementary Fig. S20. Maximum output power under various temperature differences.

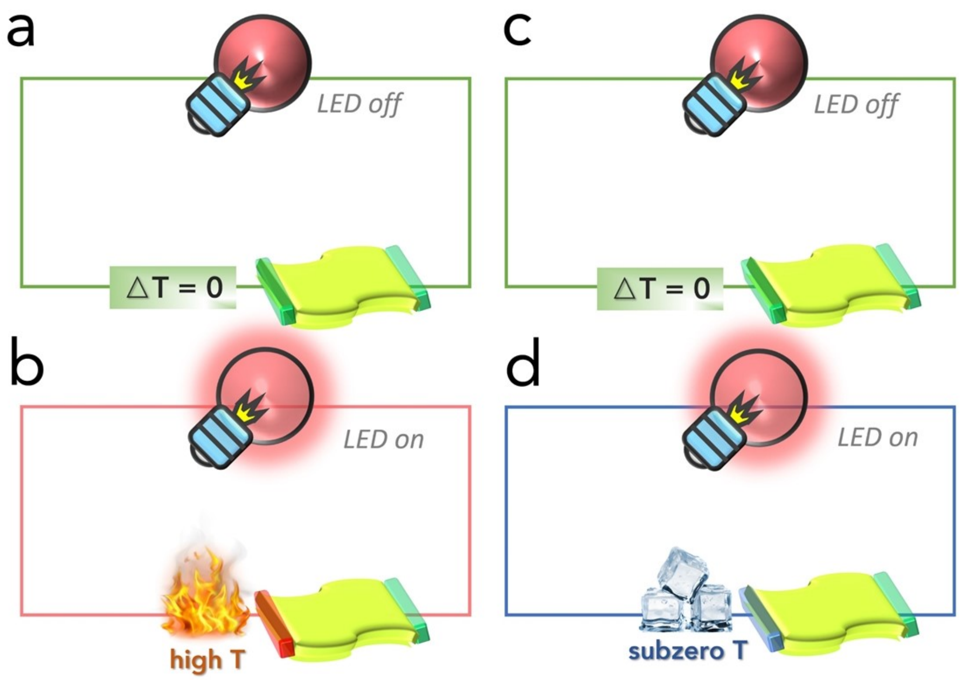

Supplementary Fig. S21. (a, b) Schematic illustration of lighting up a LED by harvesting heat energy via the temperature difference between 70 °C and room temperature. (c, d) Schematic illustration of lighting up a LED by harvesting heat energy via the temperature difference between -10 °C and room temperature.

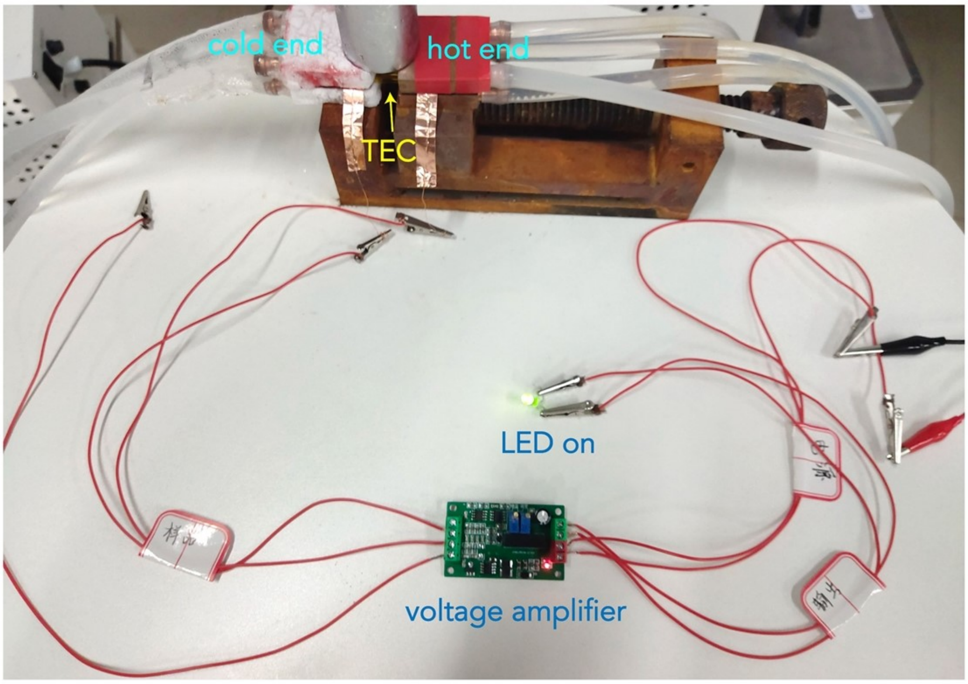

Supplementary Fig. S22. Photo showing the full setting up of using the TEC to light up a LED with the assistance of a voltage amplifier.